



ASHI: The All Sky Heliospheric Imager: August 22 – 26, 2022, NASA Balloon Flight and Image Data Reduction Analysis

Bernard V. Jackson¹ · Matthew Bracamontes¹ · Andrew Buffington¹ · Stuart Volkow¹ · Stephen White² · Mario M. Bisi³ · Edward Stephan⁴ · Philippe Leblanc⁴ · Ron Quillin⁵

Received: 11 November 2024 / Accepted: 24 February 2025
© The Author(s) 2025

Abstract

We have conceived, designed, and evaluated components for an All Sky Heliospheric Imager (ASHI), suitable for flight on future space missions both in Earth orbit and in deep space. ASHI was tested in the summer of 2022 on a NASA-sponsored topside balloon flight; in this paper, we highlight the images taken and the current state of the data reduction from this instrument's successful overnight flight. The data reduction involves the removal of starlight, zodiacal light, and atmospheric glow to enable the measurements of the outward flow of heliospheric structures. A key photometric specification for ASHI is better than 0.05% differential photometry in one-degree sky bins at 90° elongation. The ASHI balloon flight exceeded expectations and reached to a background white light level of small-scale solar wind structure variations beyond ~60° from the Sun considerably lower than this. Used as a simple, light weight (~8 kg) and relatively inexpensive spaceflight instrument, ASHI has the principal objective of providing a minute-by-minute and day-by-day near real time acquisition of precision Thomson-scattering photometric maps of the inner heliosphere over nearly a hemisphere of sky starting a few degrees from the Sun. This has large potential benefits for improving space-weather nowcast and forecast capabilities of small heliospheric structures.

Keywords Spacecraft instrumentation · Heliospheric imaging · Coronal mass ejections (CMEs)

1. Introduction

The All Sky Heliospheric Imager (ASHI) has a long heritage of instruments that image the heliosphere. Data analysis from the Helios spacecraft photometers (Leinert et al. 1975) first began this heliospheric analysis. These photometers were shown (Leinert, Richter, and Planck 1982; Richter, Leinert, and Planck 1982) to yield views not only of the zodiacal light, which was their primary objective, but also of plasma clouds in Thomson scattering brightness. These data provided rudimentary heliospheric images that extended beyond 90° elongation (Jackson 1985; Jackson and Leinert 1985). By including Solwind coronagraph data (Sheely et al. 1980) to give perspective views of heliospheric structures, the Helios photometers provided three-dimensional (3D) reconstructions of the heliosphere (Jackson and Froehling 1995). Using this previous background, the Solar Mass Ejection Imager (SMEI)

Extended author information available on the last page of the article

was conceived, designed, and constructed at UCSD, the University of Birmingham, UK, with early CCD cameras from RAL Space, UK. SMEI was launched on 6 February 2003, on a US Department of Defense test flight on the Coriolis spacecraft to Sun-synchronous orbit as a NASA and Air Force joint project (Eyles et al. 2003; Jackson et al. 2004).

The primary objective of SMEI was to use the photometric analyses from the instrument to view both corotating structures and coronal mass ejections to categorize the morphology of heliospheric structure. For the US Air Force, the objective was to forecast the arrival of these structures at Earth. SMEI viewed outward from the Sun to 180° elongation from Earth orbit over nearly 4π steradians and thus viewed the solar wind structure that passed nearby Earth. Considerable work funded primarily by the US National Science Foundation and the Air Force Research Laboratory enabled UCSD to rid SMEI images of previously unknown variable extremely high auroral light signals (Mizuno et al. 2005) viewed from its 842 km terminator orbit. This allowed low-resolution iterative time-dependent 3D reconstructions of the global heliosphere (Jackson et al. 2006; Bisi et al. 2008) and SMEI 3D reconstruction programming to be made available to the public at the NASA Goddard Community Coordinated Modeling Center (Jackson et al. 2008a). The STEREO Spacecraft Heliospheric Imagers launched on 25 October 2006 (Howard et al. 2008; Eyles et al. 2009) followed these spacecraft designs. The shortfall of SMEI was that it could at best view only within 18° of the Sun due to its rigid placement on a zenith–nadir pointing satellite. However, the STEREO HI instruments in deep space on Sun-pointing satellites were able to view within 4° of the Sun over a restricted field of view near the ecliptic.

Pertinent later to ASHI, the analysis in Jackson et al. (2008b) showed that 3D reconstructed in situ densities of a large CME and smaller solar wind structures nearby from SMEI data could be obtained from only data from 90° elongation and beyond. Jackson (2011) enabled even smaller-scale solar wind structure densities to be 3D reconstructed over time following the instrument closure. More recent analyses now use these same techniques with SMEI (Jackson et al. 2020), STEREO HI A and B imagery (Jackson et al. 2023), and Parker Solar Probe WISPR images (Jackson et al. 2024) to provide high-resolution 3D reconstructed density analyses to mesoscale heliospheric sizes (Viall, DeForest, and Kepko 2021). These now provide structure densities of $1^\circ \times 1^\circ$ in ecliptic latitude and longitude, at 0.01 AU distances, with a one-hour time cadence, and show a wealth of solar wind structure information. These analyses map the background solar wind, corotating structure, and coronal mass ejections (CMEs) outward from in situ measurements, which were never before mapped in this great detail. We intend far better analyses with a long-duration spacecraft ASHI instrument.

The ASHI instrument corral was first conceived before the period of the successful SMEI operation by the UCSD group (Buffington, Jackson, and Korendyke 1996; Buffington 2000; Jackson et al. 2010) as an advance over the SMEI instrument and has a unique design. All other heliospheric imager designs flown to date have primarily used labyrinth-style baffles to remove diffracted, edge-scattered, and spacecraft bus stray sunlight from the instrument optics. This has necessarily required a restricted instrument field of view (FOV) to cover the heliosphere close to the Sun where the heliosphere is brightest. In these instruments, very black baffling at precise strategic locations within the labyrinth removes additional stray light from entering the optical system. For ASHI, most of the stray light removal is accomplished by a circular corral surrounding the instrument, which is essentially a coronagraph external occulter extended around the optics so that only tiny amounts of diffracted light can reach the optical system. In an ideal case from a spacecraft, the Sun and any other bright light sources are hidden from the instrument lens by this curved surface. The view from the spacecraft system that holds and orients ASHI in space is then only zodiacal light, starlight,

and the two orders of magnitude fainter electron Thomson-scattered sunlight. Heliospheric imagers at 1 AU are photon-limited in viewing Thomson-scattered light. Collecting enough light beyond 60° elongation over one-hour intervals cannot be made with instruments much smaller than ASHI. Although simplified because of the necessity to fit the NASA funding call for space test instruments, ASHI was always intended for a long-duration spaceflight to accurately remove the much brighter slowly changing zodiacal light component from the imagery over long time periods. This then shows corotating structures as well as CMEs that pass the spacecraft. The ASHI design images a whole hemisphere of the sky. A single ASHI instrument system, viewing continuously with a mass total of 8 kg and an $f/1.4$ lens illuminating a current 30 mm camera chip, has an order of magnitude greater light throughput than SMEI or STEREO devices.

Section 2 discusses the ASHI instrument design and details the second ASHI topside balloon flight, which successfully took data in 2022. Section 3 discusses the steps required for the ASHI analyzed data. Some of these are unique to the topside balloon flight, but most are also necessary for use in deep space. Section 4 provides the result of the views of the background variable light during the balloon flight that reaches a level considerably below the level of heliospheric Thomson-scattered light throughout this balloon nighttime flight. This provides a view down to the level of mottled background skylight from mesoscale solar wind structure that passes Earth at this time. In Section 5, we summarize the ASHI Balloon flight and its analysis. In the [Appendix](#), we discuss the flight requirement specifications for a future long-duration ASHI Mission.

2. ASHI Instrument Design and Balloon Flight

ASHI was originally intended to be used only in laboratory tests and was begun with that concept in mind. However, through encouragement from our NASA funding agency point of contact, we applied to fly ASHI as a secondary payload topside balloon flight in early 2019, and the NASA Columbia Scientific Balloon Facility gave us a ride as soon as ASHI and the balloon were ready. The first flight of the instrument took place in the summer 2021 and was hurried to get ready during the COVID pandemic. This flight ended with several technical difficulties, and no images taken. Over the winter of 2021–2022, we refitted ASHI with a somewhat refurbished system including a better camera and a Linux operating system to replace the original Microsoft Windows 10 system controlling the camera and electronics. This new system was flown successfully as a NASA piggyback topside balloon flight from Fort Sumner, New Mexico, on August 25–26, 2022. On a balloon in Earth's atmosphere, ASHI requires a view of the whole sky with no Sun, Moon, or illuminated balloon scattering light into the FOV. At a balloon float altitude of 110,000 feet (35 km), the Earth's horizon is 6° below the horizontal, and thus lights at night on the Earth's surface are well below the 184° instrument field of regard (the horizontal across the top of the corral plus the 2° baffle curve). This flight enabled ASHI to obtain 4591 5-second images of the night sky at float altitude.

2.1. ASHI Balloon Instrument Design and Tests

Figure 1a is a schematic of the ASHI instrument that served as both a laboratory test system and for the balloon flight. Various components of the instrument are labeled. Figure 1b gives a schematic of the fisheye optical lens system illustrating various ray traces through the optics and the mirror flat at the corral edge. Figure 2 shows ASHI ready to fly from Fort

Figure 1 a) ASHI balloon SolidWorks schematic cross-section. b) ASHI balloon optics and detector schematic cross-section (the 2° corral curvature is exaggerated).

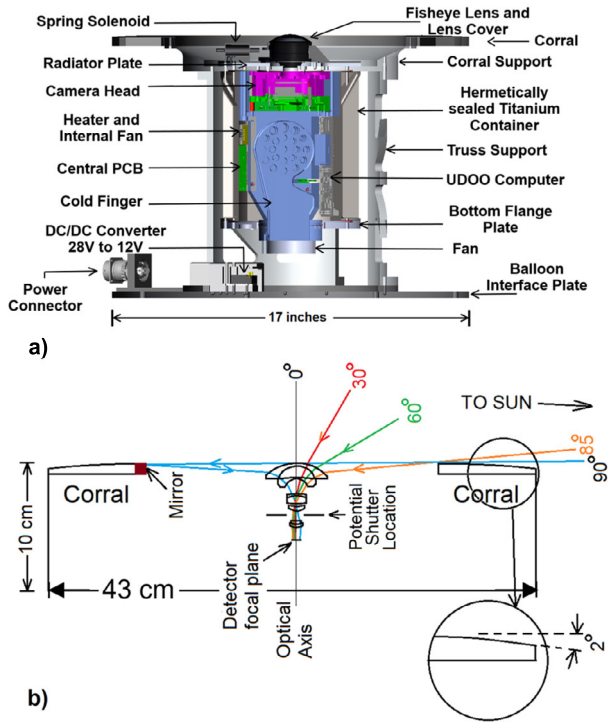
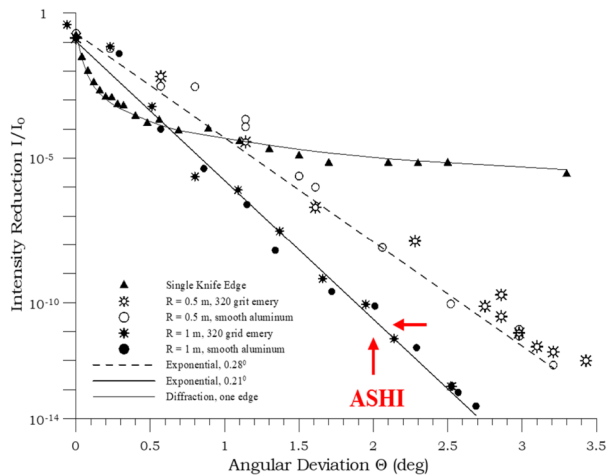


Figure 2 ASHI ready for its balloon flight.



Sumner, New Mexico. The unique ASHI design includes a corral (the white cylindrical disk at the top of the instrument). This has a 2° curved surface that reduces the light shining from below it onto the fisheye lens in the center of the corral by more than 10 orders of magnitude

Figure 3 Measured stray light rejection from curved (radii $R = 1.0$ m and 0.5 m) corral surfaces (adapted from Buffington 2000).

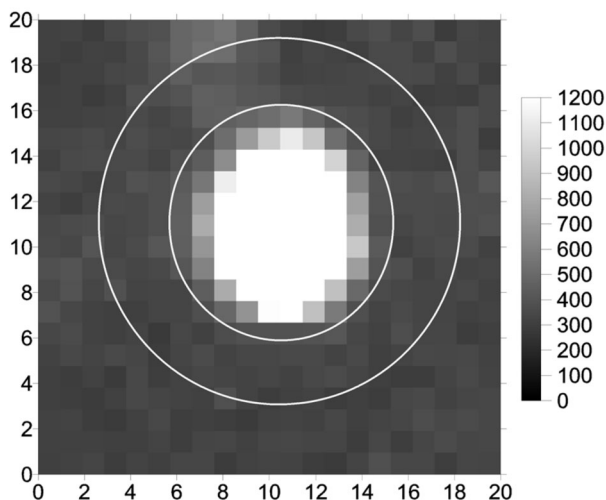


as shown in Figure 3; this system has never been flown in space before. With an accurate orientation to within $2^\circ \pm 0.1$ of the Sun–Earth line in deep space above Earth’s atmosphere, and no other bright objects in the instrument field of regard, this enables adequate solar stray light reduction on the instrument lens. With this circular corral and with the Sun below the 2° horizontal, stellar sky signals exceed the brightness of the corral edge: this design enables a low-mass instrument that nonetheless views a full hemisphere of the sky.

For the ASHI balloon flight, a second wire (in addition to the one powering the balloon valve plate) was needed for the instrument, and this required a nonstandard balloon purchase. This wire extended upward past the parachute and through the balloon from the 28-volt battery pack situated on the gondola below. The balloon standard Amphenol PT00A-16p(SR) receptacle plug for this power from the balloon to the instrument is shown at the bottom of Figure 1. A commercially purchased UDOOx86 II Ultra computer and the associated circuit boards to control the ASHI mechanisms were situated inside a hermetically-sealed 3D-printed titanium container. This was designed robustly to preserve the computer memory and an associated thumb drive that contained the ASHI image data following the balloon descent and landing at a terminal velocity of 60 feet/sec. The ASHI balloon interface plate seen in Figures 1 and 2 was a replacement for the unused topside balloon valve that required attachment to the balloon on the flight line before launch.

The ASHI balloon instrument’s second flight used a Commercial Off The Shelf (COTS) Photometrics Prime BSI CMOS camera. Although not space-qualified with rad-hard electronics, this CMOS 6.5×6.5 -micron four-megapixel (13.3 mm) chip had a cost low enough so that it could be purchased using our NASA HTIDS funding. The chip was back-illuminated, had a tested one electron read noise at -20°C , and was gratifyingly $\sim 95\%$ efficient in visual wavelengths. The manufactured camera is supplied with a thermal-electrical (Peltier) cool plate designed to rapidly decrease the instrument temperature, so that it can be used in a laboratory setup. This cool plate was a problem since the combination of a cool plate/camera/data-accumulation computer, and other ASHI electronics required more power than could be supplied from the balloon gondola to the balloon top. The Peltier cooler also formed a spacer in the camera head between the CMOS chip and the radiative camera back plate, which in the lab was cooled by a motorized fan blowing air onto the cooling vanes; this will not work at the balloon float altitude. Usually, there is enough radiative heat loss at night on a balloon top to cool the camera chip. However, the radiator to do this for ASHI

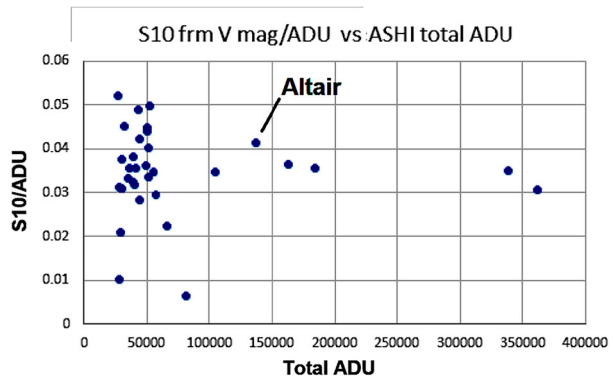
Figure 4 ASHI PSF of Altair (α Aquilae).



needed to be on the top of the system near the lens while the camera, computer, and most of the system electronics were below in proximity to the camera head cold finger inside the hermetically sealed container. The heat output from the electronic components inside the sealed container and the effect of the variable shielding of the system to the warm Earth below the balloon-top system were somewhat unknown. To be safe, we opted to replace the high-powered Peltier cooler with a version that used about one-third the wattage to cool the camera chip and also mitigate warming from the Peltier, camera, and electronics, in the interior of the titanium canister. We managed tests in the UCSD lab with a cooled evacuated chamber for small portions of the ASHI electronics and the Peltier-cooled camera head, and for the complete ASHI system, we used a larger nitrogen-purged thermal chamber at nearby Malin Space Science Systems in many-hour -70 °C tests.

Before ASHI launch, we had devised a stellar-fitting procedure that provided precise star pixel locations on each image. This allowed placement of stellar signals within a fraction of a pixel that in the case of the $2k \times 2k$ pixel Photometrics CMOS camera chip was better than $\pm 0.01^\circ$ for bright stars. To preserve the photometric accuracy for stellar subtractions, ASHI images were defocused somewhat to give as near as possible a Gaussian profile for each stellar point spread function (PSF) as shown in the Figure 4 example for Altair. The inner circle indicates the pixels included that provide those measured for stellar brightness; the outside circle is the extent of the background used to subtract from the star to determine its brightness relative to the background. Since the chip is $2k$ in size and pixels of the inner circle are 10 across, this implies stellar PSF of nearly 1° . With a CMOS camera well depth of 16 bits, none of the brightest stars and planets saturated pixels at the center of this point spread function with five-second image exposures. The focus that provides the 1° PSF is important since even with an efficient back-illuminated chip, there is a concern that chip pixel variations and dead spots will not allow stellar signals to be accurately subtracted no matter where they fall on the image plane. This needed to be tested and set before flight following transport to the Fort Sumner NASA facility for our commercially purchased $f/2.8$ LAOWA fisheye COTS lens from Venus Optics. This was accomplished at Fort Sumner, as in the UCSD laboratory, by viewing a dim stellar-like pinhole light source across a large distance in the darkened hangar facility. For stars, this fitting procedure was also useful to determine the relationship between stellar magnitude and the camera analog-to-digital response (ADU). This value is given by subtracting the numbers of ADUs per pixel within

Figure 5 ASHI camera conversion ratio from S10 to ADU is determined to be $\sim 0.035 \pm 10\%$. Stars with fewer ADUs provide a noisier signal relative to the background.



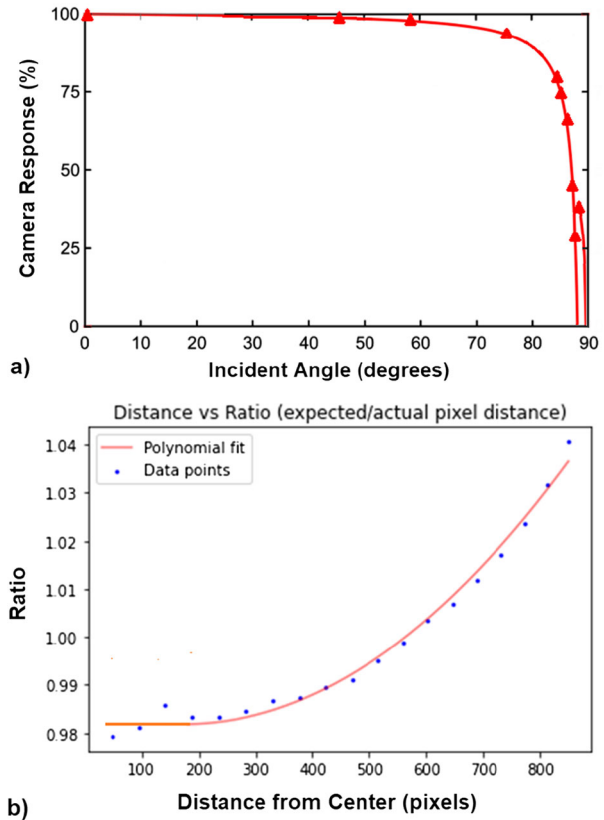
a base annulus for stars and then counting the ADUs for the whole star with this offset subtracted. This technique has been used in the past (Hick, Buffington, and Jackson 2007; Buffington et al. 2007) to calibrate SMEI and to make a comparison with coronagraph images. This was tested on ground-based stellar images to ensure we had a viable instrument before flight, since this also gives a camera brightness conversion of S10 (tenth magnitude solar-type stars in a square degree of the sky) to ADU as shown in Figure 5. This was again redone from flight images as shown in Figures 4 and 5.

Other corrections needed before the final images could be analyzed are shown in Figure 6. The first of these in Figure 6a gives the vignetting of the lens from center to edge. This was tested in two ways on the ground with both a laboratory point light source and stellar signals with different 90° rotations of the instrument over short time periods. The measured points shown are averages of these analyses. We tested the direct view of the sky from the lens, as well as that of the small mirror which provided the closest view of the Sun. The greatest vignetting is shown beyond about 80° from the lens center. We have not yet tested the image at the extreme edge of the baffle or the small mirror carefully, since the analysis from the balloon flight did not use this portion of the image in the data analysis. The displacement of imaged data from the lens optical axis shown in Figure 6b is also important in locating stars in the image data throughout the night as they move across the instrument FOV and was determined on the ground by using a large hemispherical tape measure over the optic that recorded the angular distance from the image axis in pixels. This was measured in several different angular positions around the axis and averaged. Again, this rather small distortion of at maximum 3% worked sufficiently well so that there was no issue in locating and removing stars from the image through the duration of the flight as they moved across the FOV. The mean of this at 10.4 pixels/degree becomes important to relate the S10 to ADU relationship to square degrees of the sky in the final image reduction analyses. Finally, while still on the ground and in the days before the balloon flight, ground-based twilight sky brightness measurements were obtained to determine the pixel-to-pixel variations of the CCD. These also showed a few defects on the image plane such as bad pixels and even a few larger areas like dust spots to be avoided in the combined sky maps used later following flight.

2.2. ASHI Balloon Flight

The limitation of our balloon flight, which required a strict flight window at night with no Sun or Moon in the sky, meant that we needed to be ready to fly at any available time during

Figure 6 a) The camera response to a parallel light beam (red line) mapped to the FOV incident angle from the LAOWA fisheye lens image axis. Vignetting from the corral produces sharp fall-offs for the direct view of the lens and the small mirror that peers over the edge of the corral from its opposite inside edge (smaller red line to the right). b) The mapping of the differences between the image incident angles (expected value) used to correct the pixel distance from the image center.



that window. Nearly all flights from Fort Sumner, New Mexico, begin in the morning when winds are low, and this meant that we needed to have a system that could accommodate a flight through the daytime and into the night that followed. Figures 7–12 document the beginning to end of the successful ASHI flight.

The ASHI system had a power requirement of 56 watts nominal 64 watts max, which included the modified Peltier cooler for the camera chip. ASHI could not be operated during the day with the Sun shining on the exterior surface and the inner part of the corral support, which was blackened to reduce stray starlight. Thus, for a morning flight, redundant thermal switches were installed and attached to the bottom ASHI base plate to cut all power to the system when the plate temperature exceeded 14 °C. The red-tagged pull strap on the bottom right of Figure 2 and near ASHI in Figure 7 circumvented the thermal switches and allowed the system to be tested for a short duration after power was connected in the morning on the flight line just before launch. Figure 7 shows ASHI ready to be tested following its electrical connection to the balloon gondola batteries.

A balloon flight for ASHI requires a view over the upper edge of the balloon, and the truss structure below the corral extends downward 12 inches (30.48 cm) to enable a clear view above the edge of the rounded balloon top. The distance needed for the instrument corral above the balloon was the maximum allowed by former balloon topside experience and somewhat of a guess before the actual flight. The distance needed depended not only on the roundness of the balloon at float that had been approximately calculated, but also on the rigidity of the balloon and the nearness of the protective balloon valve skirt at float altitude

Figure 7 ASHI on the flight line bolted to the balloon top and ready to go. The ASHI insulating cover is seen strapped around the ASHI support truss work, and the instrument is now ready for final electronics tests. The dust cover placed on top of ASHI is removed before flight.



throughout the flight. The surface of the Earth is 6° below the horizontal at the 35 km float altitude and thus lights on the Earth's surface at night are well below the ASHI field of regard. However, the effect of Earth's surface lights assumes that the balloon valve plate is situated at the exact top of the balloon and that the sky glow from surrounding city lights does not extend upward enough to interfere with the nighttime views.

For the balloon flight, the instrument corral support truss work seen in Figure 2 was covered by Mylar sheeting and a formed insulation buffer. This protected the balloon on launch from the corral edge and retained a temperature above 0°C for the camera and electronics during nighttime data taking. ASHI needed to be attached to the unused valve location on the flight line before the flight: This was an effort that required practice before the flight by UCSD personnel and the NASA flight crew. Following this, the insulating buffer that was made in two halves, needed to be installed above the extended power connector, and strapped into place to the ASHI exterior before launch while out on the flight line.

On August 25, 2022, wind conditions were predicted to be met for a morning launch with a set up begun well before sunrise. ASHI at a total weight of 15.8 kg and a height of 1 foot was larger and heavier than any previous instrument flown topside without a drogue balloon for initial support. Two men held ASHI to the launch table during preliminary inflation until the balloon became filled enough to support ASHI (Figure 8). When released, ASHI popped up and could be seen briefly still attached to the under-inflated balloon (Figure 9). Inflation continued with sunrise behind the balloon (Figure 10) on a beautiful day, and an easy launch release of the balloon at 6:55 am local time (Figure 11).

Thanks to a nonstandard system installed on this ASHI flight, which allowed an ASHI current supply indication from the gondola power, we were able to monitor ASHI power use in real time. Power to ASHI came on briefly as the system was cooled by the atmosphere on ascent, but shortly after reaching float altitude, the system was warmed by the Sun, and the thermal sensors cut power from the gondola to the ASHI system. ASHI continued to fly through the day until near sundown when the temperature dropped enough so that the ASHI base plate fell below $\sim 10^\circ\text{C}$, and power was restored to the ASHI system from the

Figure 8 ASHI being held down (left) on the balloon top while the balloon is being inflated by long tubes supplying the helium.



Figure 9 ASHI on top.



Figure 10 Balloon and sunrise during inflation.



base plate. At this time the ASHI computer began to operate. After the computer started, the camera turned on, the thermal-electrical cooler began to operate, and after a few unanticipated cold–warm several minute-long cycles, the system began to operate continuously until the sky became dark. When the Sun had fallen sufficiently below the ASHI corral light sensors, three of which can be seen around the inner rim of the corral in Figure 2, the dark sky triggered the fisheye lens cap to open and the camera to begin taking images. ASHI image-taking continued without interruption until power to the system was switched off after 6½ hours, just before the balloon cut-down in the early morning of August 26. ASHI attached and tangled in the balloon was recovered the next day just north of Interstate 40 near Selig-

Figure 11 ASHI on its way!

man, Arizona (Figure 12). The gondola and parachute were recovered farther north on the following day by the Columbia Balloon facility personnel.

When retrieved at the NASA facility on the way back to San Diego from Fort Sumner, ASHI was found to have received very little damage on ground impact. There were only a few scratches on one edge of the corral; the lens cover was open, and there was a slight amount of dust on the lens. From there ASHI was driven back to the UCSD laboratory. Joined by Ed Stephan in San Diego the next day and the instrument disassembled, we found the titanium canister hermetic seal unbroken and that all the electronics operated as they had before launch.

3. ASHI Balloon Data Analysis

We had no image-pointing information other than the longitude and latitude of the balloon (shown in Figure 13a), given by NASA personnel, the time of the image recorded on the ASHI camera, and the recognized stars. The analysis of the images was obtained by identifying the star Polaris from the raw ASHI images, which allowed the balloon rotation to be removed. The small 4.001 MCF ASHI balloon rotated somewhat more rapidly than we expected. Note that the north and south passages of the rotating balloon in Figure 13b indicate a wobble of about half a degree and thus a very close alignment of the balloon valve plate

Figure 12 ASHI recovery near Seligman, Arizona. The balloon valve plate cover, which has turned upside down, is seen on top with the ASHI corral resting on the ground.



to the balloon horizontal throughout the image-taking sequence. Before the balloon flight, we were also concerned that the balloon might oscillate and thus shift the stellar images in the FOV and stretch PSFs beyond their designated amounts. Although some of the slight waviness of the Figure 13b pole tracking might show this, it is usually close to the ± 0.01 PSF position resolution. The rotation rate of the balloon is shown in Figure 13c, and a few times this reached 2.0° per image frame. If continuous, this would amount to one balloon revolution in 15 minutes, and this has the potential to elongate the stellar PSFs at the extremity of the camera image. Although we can use this digital record of the balloon rotation to eliminate the most egregious rotation and obtain balloon images to the extreme edge of the camera FOV, to be expedient, this was not used in the current final analysis.

The individual ASHI fisheye images are extremely important in their own right and contain a wealth of detail throughout the balloon flight. The ASHI altitude of 35 km precluded any aircraft from being observed in the images. However, hundreds of satellites were observed in the ASHI images as streaks or moving spots of light. One of these, which is very obvious, is shown in Figure 14 as a bright streak in the whole ASHI image 581 and as consecutive bright streaks in the excerpts from the next two 5-second exposure images 582 and 583. These transient objects on one image and not another are eliminated as are cosmic ray hits or other similar artifacts in the subsequent ASHI image processing. This removes nonconformant pixel responses above and below a 3-sigma Gaussian distribution of image pixels as the data were accumulated into 50, 5-second, derotated images. As in UCSD SMEI processing, this still retains stellar and other background light sources including Thomson

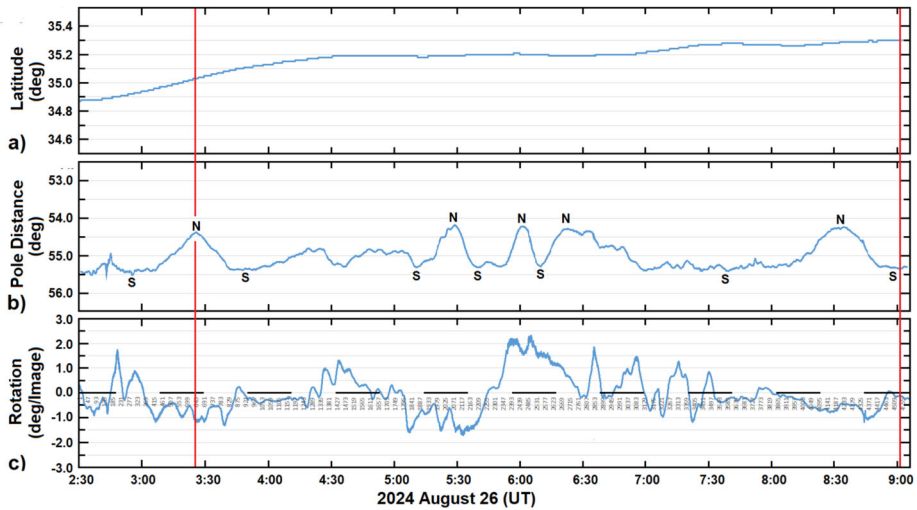


Figure 13 a) The latitude of the balloon in degrees versus UT on August 26 during the camera image-taking sequence. b) The pole distance from image center as the ASHI balloon rotated through the flight. The extrema when the image was closest north (N) and farthest south (S) are marked. Approximately half this distance is the wobble of the plate from the celestial North Pole. c) The rotation rate of the ASHI balloon in degrees per image. The small numbers on this plot indicate the image number. Red vertical lines provide the beginning and end of the period analyzed more carefully in the later Section 4 images.

scattered light but removes transient objects from the images. As in SMEI, these residual removed values are kept as images to show the location of transient objects and to check the amount of this image removal.

No processing has been done to the single image shown in Figure 14. Because a slight remnant of twilight is present to the lower right in this early image, these early images were unused in the final data reduction, which began five minutes later. The lens images the inside of the blackened corral that can be seen faintly at the image's outer extremity. The illumination here is primarily from starlight with a level of ~ 150 ADU (5.25 S10) per pixel and is much dimmer than the background stars, contributing an insignificant amount of scattered light onto the image plane. There is also a patch of sky with some stars present in the vignettted view from 2 to 3 o'clock, which is from the small mirror used to extend a patch of sky nearer the Sun from a long-duration spacecraft flight. The stars near the edge of the image are slightly elongated due to the rotation of the balloon. There were also several detector blemishes seen, and while individual images were available, the image pixels were flat-fielded to remove the pixel-to-pixel variations determined before flight. A few dust spots and two larger blemishes on the chip were removed by a cookie-cutter technique that eliminated them from the derotated images.

When we imaged the balloon data as in Figure 14 or 15, we noticed a brightness increase all around the image edge. We did not anticipate airglow to be a problem until we looked more carefully at the Photometrics CMOS chip specifications. Indeed, there is a note that this specific chip has some small sensitivity to ultraviolet light where there is a dominant airglow contribution. With airglow present, it is reasonable to assume that this would be brighter near the horizon where more atmosphere is traversed along any given line-of-sight (LOS). This tended to be fairly uniform and mostly present at the extreme edge of the image from the beginning to the end of the $6\frac{1}{2}$ -hour observing sequence. At the beginning of the

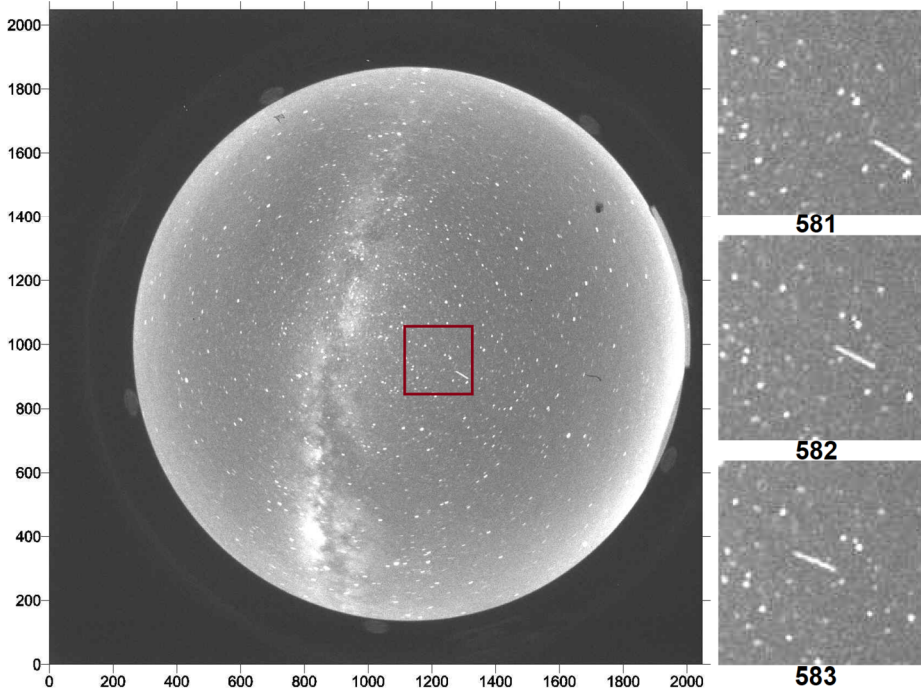


Figure 14 ASHI fisheye image 581 with insets of a highlighted 24° patch of the sky to the right showing a close-up of this and two following images of a bright Earth-orbiting satellite streak. The inset images also show a mottling caused by the many stars in the individual images, which must be subtracted to enable the Thomson scattering signal to be discerned.

Figure 15 Derotated 50-image data set (images 5150 – 5199) with the celestial pole placed at the image top exactly north of the image center. Polaris is shown. A slight glow around the periphery of the image can be discerned in the image that is cropped by 5° from the image edge to remove the most egregious airglow.

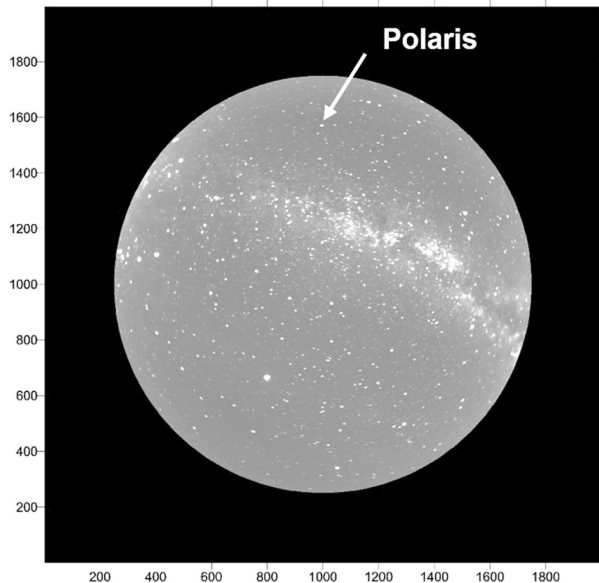


image analysis, we used our stellar position determination to remove the balloon rotation by locating the nearby celestial north pole in the image from Polaris so that the polar location was placed directly north of the image center as shown in Figure 15. In subsequent images used for the balloon flight analysis, images were cropped 5° from the outer edge. Airglow had a level from about 50–100 ADU per pixel from the portion of the image edge used at 82° to the image center at 0° or 1.75–3.5 S10 per pixel as seen in Figures 14 and 15 and was considerably below the average background Milky Way brightness enhancement. Both light sources have been almost completely removed in the subsequent images used in the final balloon flight analysis.

At this stage, in the images, we looked for but could not observe the upward streaks in the Polar Regions seen in the SMEI data during periods of geomagnetic activity (Mizuno et al. 2005). At times, these illuminated the whole sky around SMEI in its 842 km orbit and could be seen extending upward to over 10,000 km above Earth with a brightness several hundred times that of the Thomson-scattering signal near the spacecraft that would have been as bright as the airglow but seen as streaks. First observed in SMEI associated with auroral activity, these bright streaks were later attributed to an upwelling of N_2^+ ions studied close to the ground (Hunten 2003) and an upwelling of these ions to large distances from the Earth was ascribed by Lummerzheim et al. (2008). Potentially ubiquitous, although faint, we were concerned that this variable brightness would be present in all of the ASHI images. The ASHI balloon images were viewed to ~ 500 km above the Earth's auroral oval to the north, and these streaks could extend upward over 75° above the ASHI field of view edge. There was little geomagnetic activity during the ASHI balloon flight, and there were no noticeable bright upward light streaks observed. However, for any low near-Earth imaging system, this needs to be contended with as a large-scale variable source of solar-type brightness. This bright upwelling would certainly have been observed during geomagnetic storms from a balloon ASHI and may be a motive to fly the instrument again at times of high geomagnetic activity to explore this phenomenon.

To remove airglow, we developed a smooth large-scale filtering system mask, which removed all bright point sources with the images oriented north–south. This was accomplished by combining celestial pole-rotated images over time and filtering each image set to provide a template without stellar and other bright or dark residuals. This template was then subtracted from the original data to remove the airglow from all the derotated and recentered ASHI image sets used in further analyses. With the rotated camera images, removed of most of the airglow and cropped at the edges by 5° where the airglow was greatest, we could provide much cleaner sky maps, where stars could be subtracted without this image periphery brightness present.

The balloon images that were oriented north–south then needed to be placed into Right Ascension (RA) and Declination (Dec) coordinates. To do this, the UT time and Earth longitude provide the sidereal time and the position of the north–south meridian when the image was obtained. With the celestial pole and south direction known, each image was reoriented in terms of the same celestial meridian as the sky passes above the balloon camera fisheye lens. Interpretation of the fisheye lens view from these images into a spherical projection then proceeds, as, for instance, Bourke (2016) and others describe. Then, the center of the image provides an axis of the image's spherical projection. An Euler angle rotation of the image center from the celestial pole places the lens' spherical coordinate projection of the sky into RA and Dec coordinates. When completed for each image, this analysis allows all images to be combined so that stars in the images are accumulated in the same sky locations. The combined individual images can then be placed into different forms of sidereal, ecliptic, or heliographic coordinates.

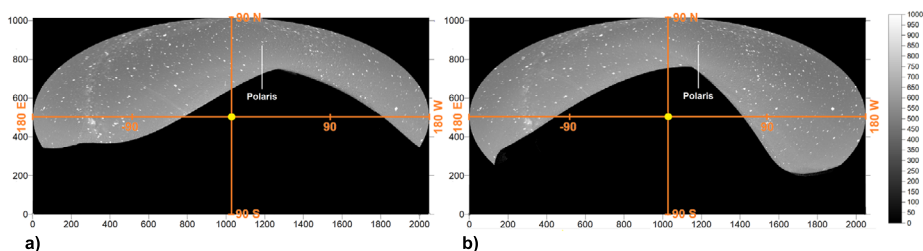


Figure 16 a) Imaged data set (images 401 – 2000) and b) (images 2001 – 2790 and 2901 – 4520). The location of the Sun (center, yellow) and Polaris are shown. The image scale to the right is in ADU.

4. Balloon Imaging Results

Throughout, from the first images to the end, all valid ADU values were collected and accumulated, averaged by the numbers of hits in a given bin. In this way, the S10 to ADU conversion can be kept throughout all the analyses, including image differencing. Once the balloon images are placed into sidereal coordinates and accumulated over the balloon flight, they can be dealt with in more detail, just like the images from SMEI. However, unlike the SMEI data, for the short duration of the balloon flight, there is no possibility of removing a long-term base from the images that includes a zodiacal light component. Thus, in the following analysis, zodiacal light is assumed to be approximately constant in sidereal coordinates over the selected period of the balloon flight. The zodiacal light component that moves roughly $1/4^\circ$ relative to the sidereal component is small and can approximately be removed by filtering techniques that eliminate the east–west differences in longitude brightness across the image. The individual images had 2048×2048 pixel binnings. Thus it made sense to place the data from each pixel into the corresponding sky bin of another system, add up the numbers of ADU values placed into the bin, and divide this by the numbers of times this occurred, to get an average number of ADU in any given pixel. This preserves the same approximate resolution of the original image and the numbers of ADU in a bin. In Figure 16 the composite images have been turned into Hammer–Aitoff projections of the whole sky in ecliptic coordinates, which conserves areas of the sky over the image extent. As an exploratory analysis, we determined that twilight and the zodiacal light component were still too bright in the beginning images and subsequently began the reduction at image 641, over 15 minutes later than shown in Figure 14. Although we removed the time of higher rotation in these images during the latter half of the imagery (images 2791 – 2900 \sim 6:30 UT to \sim 6:40 UT, see Figure 13) we found that this made little difference in the overall binning in our cropped images and did not explore this type of whole image removal further. In the ongoing analysis, using the previous steps in image processing, we accumulated the images and converted them into heliographic coordinates as shown as an example in Figure 16. In these image maps the Milky Way is east of the Sun and loops around to the west of the Sun, with fewer stars. The overall brightness of the Milky Way is attenuated here by the mask used to remove airglow. In these Sun-centered images, the extent of the image obtained of the night sky from the balloon in Figure 16a shows more of the sky to the east of the Sun. In Figure 16b, more sky is available to the west of the Sun as the Earth rotates away from sunset. To obtain sky views devoid of stars that retain the most background Thomson-scattered light, they must be subtracted using the bulk of the images consistently present in the FOV. Stars do not subtract completely since they are not reproduced exactly from image to image.

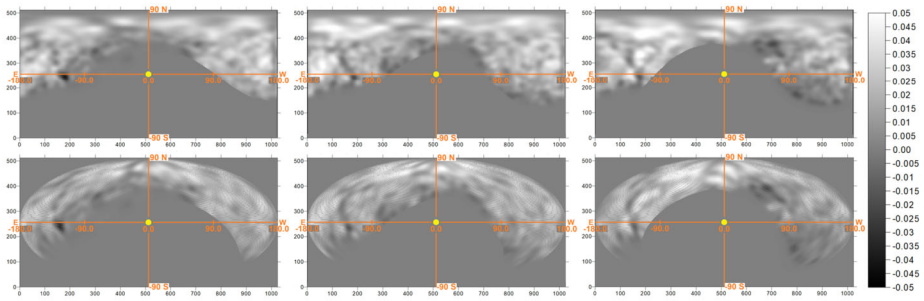


Figure 17 Cylindrical (top) and Hammer-Aitoff (bottom) views of 1300 images each beginning on image 641, 1941, and 3241 left to right respectively subtracted from the mean of the 3900 images. The location of the Sun is shown. The image scale to the right is given in S10 units.

This results from the balloon rotation, image misalignment, the dead spaces between pixels, and pixel outages caused by image defects incorrectly removed by image flat-fielding. These leave plus or minus residuals when they are subtracted from one another. We found this made little difference when these images were included in the analyses of Figure 17. Most details of this data reduction were experimented with before the ASHI flight in ground-based images. These analyses were deemed good enough to provide the accurate removal of all but the brightest stars and show Thomson scattering signals below the level required to view the heliosphere from ASHI in space. However, it was not until the balloon images were available that the total effect could be determined.

The first analyses of these images presented at Solar Wind 16 (Bracamontes et al. 2023a) showed a change across the image of about one S10 unit. We presume that most of this large longitudinal difference was caused by the two-order-of-magnitude higher zodiacal light brightness that could not be effectively subtracted by image differencing. Binned, again with the numbers of ADU preserved and ADU numbers changed into numbers per square degree, our images were further dealt with more completely using heliospheric cylindrical coordinates. We then employed the Fortran algorithm gridsphere3d (Hick, Buffington, and Jackson 2005) from the SMEI analyses and other data sets, available in SolarSoft, to remove and replace stellar residuals using a circular Gaussian filter, 1° in $1/e$ size, from subtracted images. In addition, large variations greater than 50° $1/e$ in size were also removed from the differenced images. This eliminated both the large variations and the small speckling of the imaging caused by the stellar subtraction. When three sets of evenly spaced images were subtracted from the normalized sum of all the images and converted to S10 units as shown from the Figure 5 conversion, this resulted in the three views shown in Figure 17 in both cylindrical coordinates and as Hammer–Aitoff projections (Bracamontes et al. 2023b). The variation of the pixel differences from the mean for the center map difference image is shown in Figure 18. These differences show the extrema from the mean of all known nonzero pixels where each of the original image pixel values has been combined into groups of four. This analysis shows a variation for all valid combined pixels that on average are about ± 0.015 S10 with an extreme excursion of about 0.025 S10 from the mean over the whole of the image. For each image, it was important to include as many pixels as possible to reduce the image noise level from camera background effects such as read noise, shot noise, and inaccurate stellar response from the CMOS chip inter-pixel dead spots. While there are sufficient numbers of pixels to accomplish this 180° from the Sun, it is at the image edges closest to the Sun and at the southern extremity of the images, where this number of illuminated pixels over any given time decreases significantly. Thus this effectively limits

Figure 18 Histogram of the differences of the ASHI center data set of 1300 images subtracted from the mean of 3600 as given in Figure 17.

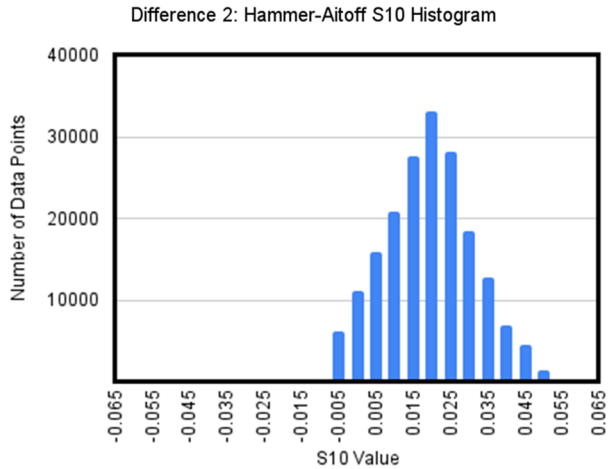
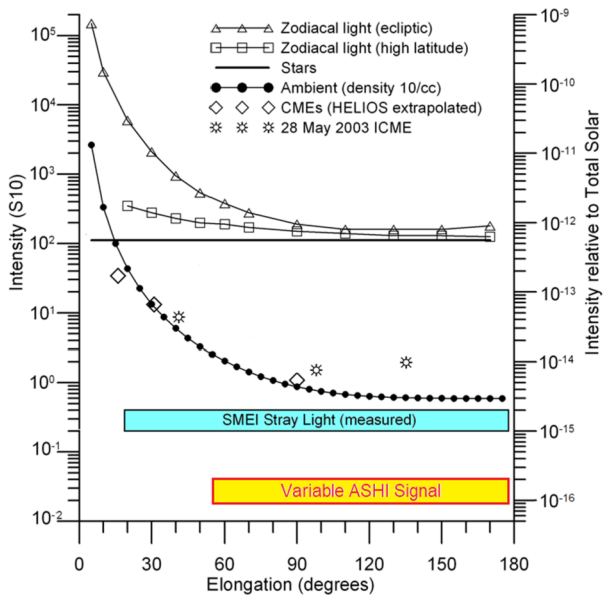
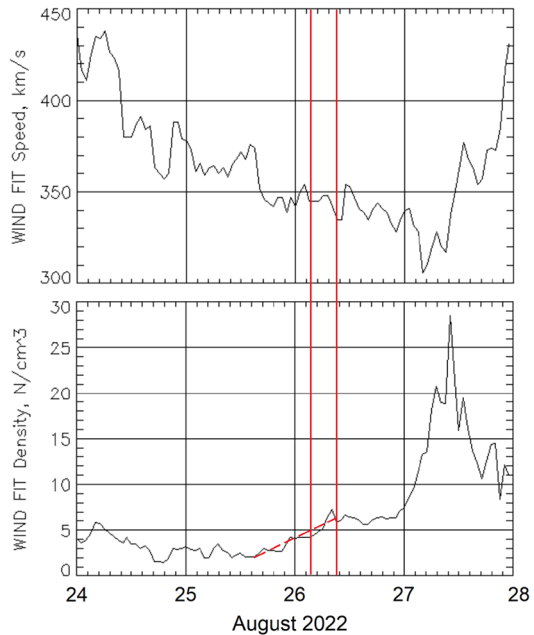


Figure 19 Brightness of the sky in S10 units. The dotted curved line gives a value about a factor of two greater than the usual solar wind mean of $\sim 5 N_e \text{ cm}^{-3}$ at 1 AU. The yellow box at the bottom of the graph is the approximate maximum difference value of the ASHI background at ~ 0.025 S10 unit.



the ASHI balloon images to locations from over $\sim 60^\circ$ of the Sun outward to 180° and to not much farther below the northern hemisphere. At these locations, the images become an indistinct blur. However, there is much structure in the difference images, and when these are played in an animation (see <https://ashi.ucsd.edu>, the “system” dropdown and “data analysis”), some of the structures appear to move outward from the Sun shown at the center of each map. This can be compared with the known brightness of the background solar wind as in Jackson et al. (2010) and repeated here in Figure 19 with an extension of the scale at the bottom of the figure that shows this variable signal. This signal is considerably lower than that from any previous heliospheric imager flown; the only other imager that looked at more than 90° elongation was SMEI, and it is worth taking a closer look to understand the ramifications of this signal.

Figure 20 Wind spacecraft instrument time series of the proton solar wind velocity (top) and density (bottom) passing Earth from August 24 – 28, 2022. The red vertical lines indicate the 6-hour time interval over which ASHI observations were analyzed, as shown in Figure 17. (Wind data courtesy of the NASA Space Science Coordinated Data Archive).



At this time, there was no known CME or large density enhancement present in the solar wind near Earth, and the background given by the Wind spacecraft (Ogilvie and Desch 1997) was $2.0 - 6.0 N_p$ before and throughout ASHI observations shown in Figure 20 by the red upward-sloping dashed line. This indicates a very low level of solar wind density and velocity and its variation in the one-hour averages of the solar wind that passed Earth during this period. The fact that the variations are noticeable and that there is a change from one differenced composite 1300 image set to the next at a low level is a testament to the excellent ASHI instrument performance from its balloon-top vantage point. A calculated typical smooth Thomson scattering brightness signal at 1 AU from an r^{-2} heliosphere of $10 N_e$ at 1 AU (Figure 19) gives a constant electron brightness of about $2.0 - 0.5 S_{10}$. The variable ASHI signal is $\sim 0.025 S_{10}$ over the bulk of the antisolar elongation range or about $1/20$ of this or $0.5 N_e$ (or N_p assuming that the number of electrons in the solar wind associated with Helium ions is insignificant). The variations above the mean (the upward sloping red line with time) of solar wind proton density indicates hour difference variations over 6-hour intervals both several days before and one day following of about $1.0 N_p$ with an ever-increasing upward trend in density before a large solar wind structure that arrives at Earth about two days later. At this speed, solar wind structures of 0.22 AU take about a day to pass Earth, and the fall-off of LOS significance over this distance past Earth decreases by factors of two or three depending on the antisolar location of the structure. If the solar wind structures are radially coherent during the ASHI observation interval and have moved outward radially, only densities before and during the observation times give variations that will effectively provide the S_{10} variations observed. Given that a LOS traverses the solar wind over several of these variations, and the in situ measurements of the variations indicate structures on the order of $0.05 - 0.10$ AU in size, the actual LOS brightness variations would be somewhat decreased in amplitude. Thus this almost exactly matches the variation of structure brightness seen passing Earth at this time, confirming that the structures seen are indeed likely those from the solar wind. *If so, these are the first brightness images obtained*

so far of the small-scale (mesoscale) structure (see Viall, DeForest, and Kepko 2021) in the background solar wind that passes nearby Earth and moves outward in the antisolar direction. Thus this indicates that at 1 AU distances, the solar wind is mottled and corrugated not only for the larger CME structures as shown in SMEI data (Jackson et al. 2020, 2023), but also for those solar wind structures that are smaller with presumably different speeds as shown in situ.

5. Balloon Flight Summary and Conclusions

We were extremely fortunate to have had a long balloon flight into the night for ASHI with no Moon and Sun in the sky to hinder observations. This has allowed a 6¹/₂-hour period from which we can certify the ASHI operation. The ASHI operation requirement for a flight with no Moon and Sun in the sky produced a flight opportunity window that was rather narrow. This was predicated not only by low winds at launch, but also winds aloft in the correct direction so that the balloon would not travel outside boundaries into a restricted area on Earth or to a place where the flight crew was unable to monitor and cut down the balloon. In the end, we took a chance that all would work well enough for a flight, and we were extremely lucky in this. This second flight worked well; the instrument performed exactly as expected both in prior tests at the NASA facility in Fort Sumner and during flight. Given ASHI recovered with little damage, we still have an instrument that we can test and show to this day.

The ASHI data analysis has taken place slowly. Some of these steps are specific to the balloon, such as the need to derotate the images and remove airglow. Adequate removal of the airglow was accomplished by slightly cropping the near-horizon signals. This will not be needed in a space flight. If airglow had contributed significantly to the background brightness variations on the balloon flight, it would have been observed as unexpected brightness variations on the inside edges of the ASHI FOV near the Sun in Figure 16, but it was not. We also did not see any evidence of a bright rim of light on the corral edge just after sunset, which would indicate something amiss with the never-before flown corral curved baffle. Since scattered starlight did not overwhelm the ASHI solar wind observations, this also certified the use of our small ASHI LAOWA fisheye lens. The balloon flight did not allow many options for extreme lens cleanliness other than a careful wipe of dust the day before launch, covering the lens with a nonairtight cover, and then a Styrofoam cover over the entire ASHI corral until its removal by NASA personnel on the flightline before launch. This did not significantly affect the scattering of starlight from the lens into the FOV. We have not yet tested the small mirror images intended to look over the corral from its other side allowing the nearest view of the solar limb as possible for this system. Indication that it worked can be seen in Figure 14 on the right side of the full image as a small strip with a few stars reflected in it. This mirror image is very dependent on the lens and its vignetting for viewing close to the Sun, and different lenses and cameras used on a spaceflight will need to be carefully tested and adjusted prior to flight.

We have preserved the numbers of ADUs present throughout our rebinning analyses, and thus our comparison of ADUs to stellar brightness allows for a determination of the ADU camera values and their variations in terms solar brightness in a square degree of sky throughout. The most significant discovery is that our balloon flight images for the first time has reached the level of the background solar wind electron Thomson-scattering brightness for those structures that pass Earth at 1 AU and continue to flow outward in the antisolar direction. The structures observed in these images are not smooth but are patchy

and mottled, and since we have gotten down to the level of brightness density variations in the solar wind, it is highly likely that these are from actual solar wind variations. If this patchiness is caused by the solar wind background density variations, it indicates that both the background solar wind, and as shown previously, the patchy large CME structures and shocks that pass 1 AU (Jackson et al. 2020, 2023) have this characteristic. It then remains to determine whether both are caused by the same processes.

In summary, for the first time, we have been able to view the level of background solar wind mesoscale structure passing the spacecraft and have certified the ASHI instrument utility to fly in space for a sustained period. This analysis has demonstrated the ASHI ability to deliver a low brightness level that will provide remote sensing of small-scale structure variations to extrapolate measurements from in situ monitors into the space surrounding the spacecraft.

Appendix: ASHI as a Long-Duration Spacecraft Instrument

The ASHI instrument, its programming, and data analysis have all been intended eventually for a flight into deeper space than a balloon and on a longer-duration flight. With a larger fisheye lens and a suitable non-COTS camera with a larger detector within the same ASHI housing, this will enable an order of magnitude more throughput than SMEI or STEREO to reconstruct the heliosphere in 3D over time in high resolution.

Work on ASHI began in earnest when we first received 4-year grant funding from the NASA Heliospheric Technology and Instrument Development for Science (HTIDS) program to build and test ASHI in late 2016. Our NASA funding for building the instrument and its testing were predicated by the eventual use of ASHI in a long-term spaceflight. ASHI is designed to eliminate the shortfalls of both SMEI and the STEREO spacecraft imagers in that the system will look as close as 2° of the Sun and out to 180° from it in a single image providing a global view of the solar wind brightness changes that pass the instrument. If the instrument is rotated around the Sun–spacecraft line, then a single system can view nearly the whole sky. We originally intended to only carefully test the experiment on the ground and then at our lab, and we felt there was no possibility to test ASHI on a balloon gondola (the balloon was in the way) or on a rocket flight (the duration of rocket flights is too short and ASHI's size too large). However, encouraged by NASA personnel to explore the possibility of a topside balloon flight, we proceeded in the second year of the contract with the possibility of testing ASHI in this manner.

The ASHI balloon lens and camera were acquired using funding from the NASA HTIDES program. With a larger $f/1.4$ custom lens illuminating a 30 mm large well depth CCD chip, vast improvements are possible in long-term near-Earth heliospheric analyses. Here a relatively simple system will allow for timely 3D reconstructions of small scale solar wind densities and velocity structures that pass the spacecraft. While the evolution of solar wind structures that pass the spacecraft at 1 AU is an interesting scientific study in itself as shown from the balloon ASHI instrumentation, the system will provide vast potential improvements in space weather forecasting and nowcasting capabilities if the instrument is situated near Earth. On an existing spacecraft with an appropriate Data Handling Unit to access the camera images, compress them, and with an appropriate downlink capability to transmit them to the ground with low latency, we estimate the instrument to require 12 watts nominal, 15 watts peak power, with standby power of 3 watts. Table 1 provides an ASHI tentative mass budget summary for the instrument and its various parts based on the

Table 1 ASHI Experiment NTE mass summary

Experiment component	Mass estimate, kg	Allocated margin, kg	NTE total mass, kg
Corral	1.5	0.23	1.73
Baffle, Corral Support	0.5	0.08	0.58
Radiator	0.5	0.08	0.58
Primary Optic Cover	0.3	0.05	0.35
Camera Container	0.5	0.08	0.58
Fisheye lens & Housing	1.5	0.23	1.73
Camera, cold finger	2.5	0.05	2.55
Total Mass, kg	7.3	0.80	8.10

NASA Small Explorer Polarimeter to Unify the Corona and Heliosphere (PUNCH) mission (DeForest et al. 2022) camera and the larger custom lens needed to illuminate it fully.

The ASHI spacecraft system can be placed in a variety of orbits from Low Earth Orbit (LEO), Geosynchronous Orbit (GEO), L_1 orbit, or in deep space. In LEO the ASHI system is not too efficient since it needs to view the sky close to the Sun and away from Earth with no bright Moon in the sky. In an equatorial LEO, which takes about 120 minutes to complete, this would allow for a view of the sky close to the Sun for only half a month to eliminate the Moon on the opposite side of the sky. There is only a short period per orbit where the system would remain at a location where it could view within 2° of the Sun during this half month. With short exposures (5 seconds, like in the balloon experiment), following the close view, it would be possible to continue exposures when the Moon is not in the field the view. A LEO Sun-synchronous polar orbit is better for a more continuous close view of the Sun in a Sun-pointing system. In this type of orbit, the Moon is still a problem since there are times, especially when the Moon is full, that it cannot be eliminated from the sky in a view away from Earth, and there are also times when the Earth eclipses a near-solar view. Both LEO orbits will need to deal with the bright aurora at times when there is significant geomagnetic activity, but the aurora can be somewhat better removed than in SMEI since minimum map image techniques using successive images will allow for clear views of the same area of the sky from different orbital locations. All of these systems require the spacecraft holding ASHI to be constructed so that the spacecraft itself does not intrude into the ASHI field of regard during the image exposures.

Views of the whole sky get better from GEO orbit and others farther from Earth. From GEO, Earth subtends 17.4° , is very bright, and it and the Moon need to be eliminated from the ASHI view. In this orbit, the Earth, the Moon, and the Sun can be thought of as a three-object plane, so as long as any of these objects are out of the FOV with the instrument preferentially pointed within 2° of the Sun, that portion of the sky can be observed continuously. GEO orbits are not always in the equatorial plane, but on average, a single ASHI rotated Sun-pointing system will be able to obtain alternate views of nearly the whole sky once a day in long-duration exposures. From GEO orbit, the Earth's aurora will no longer be a problem, and the upwelling of N_2^+ will be an interesting effect to study during geomagnetic storms from this vantage point. At L_1 , both the bright Earth and the Moon are sometimes in the field of view during the orbit. However, our calculations show that both Moon and Sun can probably be eliminated from the view by a mask that hides views of either from illuminating the detector directly and appropriate baffling on the side of ASHI nearest the Sun to reduce the light from the Earth or Moon from scattering back into the lens from the

solar direction. In a 2007 NASA Small Explorer proposal, two ASHI systems were mounted on opposite sides of a Sun-pointed spacecraft to view the whole sky without it being rotated.

In short, we expect that the ASHI instrument will find acceptance on many spacecrafts that can accommodate its design because of its large field of view essential for the most complete solar wind plasma viewing, low mass, and the ability to extrapolate data from in situ monitors into the region of space surrounding the spacecraft. The ASHI instrument should be flown near Earth where it will provide the necessary complete Sun to Earth 3D reconstructions of evolving transient and corotating solar wind structures down to mesoscale sizes.

Acknowledgements ASHI was designed and constructed by a team of scientists and engineers from the University of California at San Diego. The ASHI instrument and the data analyses presented in these studies were managed entirely by UCSD. We acknowledge NASA grants NNX17AG13G and 80NSSC22K1907 for ASHI construction and data analysis from AFOSR grant FA9550-19-1-0356 in the early stages of the image reduction of this effort. M.M.B. also acknowledges support via the RAL Space In-House Research programme funded by UKRI STFC (award ST/M001083/1) and the Space Weather Core Funding from UKRI STFC. Access to the many of these same images and videos of the ASHI flight as well as ftp access to the entire ASHI 4591 image data set are available through the website: <https://ashi.ucsd.edu>. Special thanks are due to our NASA sponsors and NASA point of contact Dan Moses who led us to the concept of implementing ASHI on a test balloon flight following its initial funding, and for both Dan and Roshanak Hakimzadeh for persevering through several extensions of the initial grant until the balloon ASHI was flown successfully and the images tested. Kudos are also needed for the group at Fort Sumner, New Mexico, for their excellent help in the ASHI balloon flight success of August 25 – 26, 2022. We acknowledge the Wind data used in our balloon analysis from the NASA NSSDCA. We also gratefully acknowledge Dr. Paul Hick who pioneered the SMEI analyses at UCSD, and who contributed much of the previous pathfinder data analysis for this earlier instrument that has been used to some extent here. Additionally, we want to honor the memory of Dr. Stephen Kahler who was the earlier Air Force sponsor of SMEI, and persisted at AFRL, New Mexico to help sponsor ASHI for the United States Air Force. We are also thankful for the encouragement and help of many other UCSD students, staff, and contractors who have contributed to the success of the ASHI balloon-flight instrument.

Author contributions B.V.J. led the group in the construction of ASHI, in engineering, and optical tests, and balloon flight-line tests. Following, he subsequently provided much of the analysis programming that reduced the camera images from the balloon-borne system into their final digital formats. M.B. helped in the early construction of ASHI, designed portions of the system in SolidWorks, provided tests of the optical system, programmed the ASHI flight computer, helped insure system operation at prior to balloon flights and flight-line tests. Following the balloon flight he also provided much of the analysis programming of the ASHI images. A.B. provided and tested the ASHI curved corral long before the proposed effort began, and continued advice on the optical properties of the ASHI camera image reduction and stellar removal during instrument testing. S.V. has acted as Program Manager for ASHI in the later portions of the flight construction of the instrument. S.W. is the current AFRL representative who has helped the P.I. present ASHI for a spaceflight on a DoD satellite. M.M.B. helped in the original ASHI instrument design and has acted as an advisor for the ASHI instrument throughout its development now as Head of UK Space Weather at UKRI STFC RAL Space. E.S. is the senior engineer responsible for the detailed design, operation and construction of the ASHI instrument electronics, and was present for flight tests that assured ASHI operation before each NASA flight. P.L. provided the SolidWorks mechanical design of ASHI for laboratory tests and these were later modified by him and seen through to their construction for the balloon flight. R.Q. helped in providing critical portions of the ASHI camera, computer and balloon electrical interface connections and soldering, and in final thermal qualification tests of ASHI at Malin Space. All authors were sent and received the manuscript to review.

Data Availability As stated in acknowledgements: Access to the many of these same images and videos of the ASHI flight as well as ftp access to the entire ASHI 4591 image data set are available through the website: <https://ashi.ucsd.edu>.

Declarations

Competing interests The authors declare no competing interests.

Open Access This article is licensed under a Creative Commons Attribution 4.0 International License, which permits use, sharing, adaptation, distribution and reproduction in any medium or format, as long as you give appropriate credit to the original author(s) and the source, provide a link to the Creative Commons licence, and indicate if changes were made. The images or other third party material in this article are included in the article's Creative Commons licence, unless indicated otherwise in a credit line to the material. If material is not included in the article's Creative Commons licence and your intended use is not permitted by statutory regulation or exceeds the permitted use, you will need to obtain permission directly from the copyright holder. To view a copy of this licence, visit <http://creativecommons.org/licenses/by/4.0/>.

References

- Bisi, M.M., Jackson, M.M., Hick, P.P., Buffington, A., Odstroil, D., Clover, J.M.: 2008, Three-dimensional reconstructions of the early November 2004 coordinated data analysis workshop geomagnetic storms: analyses of IPS speed and SMEI density data. *J. Geophys. Res.* **113**, A00A11. DOI.
- Bourke, P.: 2016, Converting a fisheye image into a panoramic, spherical, or perspective projection. Online at <https://paulbourke.net/dome/fish2/>.
- Bracamontes, M.T., Jackson, B.V., Buffington, A., Volkow, S., White, S., Bisi, M.M., Stephan, E., Leblanc, P., Quillin, R.: 2023b, All Sky Heliospheric Imager {ASHI}: First Near-Ground Imager to View the Interplanetary Medium 90 Degrees from the Sun and Beyond. *Oral presentation in session SH32B at the AGU conference, San Francisco, California, 11 – 15 December*.
- Bracamontes, M.T., Jackson, B.V., White, S., Bisi, M.M., Buffington, A., Volkow, S., Stephan, E., Leblanc, P., Quillin, R.: 2023a, ASHI: All Sky Heliospheric Imager: August 25 – 26, 2022 NASA Balloon Flight and Image Data Reduction Analysis. *Solar Wind 16 poster and flash talk presentation, Asilomar, CA, 12 – 16 June*.
- Buffington, A.: 2000, Improved design for stray-light reduction with a hemispherical imager. *Appl. Opt.* **39**, 2683. DOI.
- Buffington, A., Jackson, B.V., Korendyke, C.M.: 1996, Wide-angle stray-light reduction for a spaceborne optical hemispherical imager. *Appl. Opt.* **35**, 6669.
- Buffington, A., Morrill, J.S., Hick, P.P., Howard, R.A., Jackson, B.V., Webb, D.F.: 2007, Analysis of the comparative responses of SMEI and LASCO. *Proc. SPIE* **6689**, 66890B-1.
- DeForest, C., Killough, R., Gibson, S., Henry, A., Case, T., Beasley, M., Laurent, G., Colaninno, R., Waltham, N., the PUNCH Science Team: 2022, Polarimeter to UNify the Corona and Heliosphere (PUNCH). In: *IEEE Aerospace Conference (AERO)*. 978-1-6654-3760-8/2. DOI.
- Eyles, C.J., Simnett, G.M., Cooke, M.P., Jackson, B.V., Buffington, A., Hick, P.P., Waltham, N.R., King, J.M., Anderson, P.A., Holladay, P.E.: 2003, The Solar Mass Ejection Imager (SMEI). *Solar Phys.* **217**, 319.
- Eyles, C.J., Harrison, R.A., Davis, C.J., Waltham, N.R., Shaughnessy, B.M., Mapson-Menard, H.C.A., Bewsher, D., Crothers, S.R., Davies, J.A., Simnett, G.M., Howard, R.A., Moses, J.D., Newmark, J.S., Socker, D.G., Halain, J.-P., Defise, J.-M., Mazy, E., Rocus, P.: 2009, The heliospheric imagers onboard the STEREO mission. *Solar Phys.* **254**, 387.
- Hick, P.P., Buffington, A., Jackson, B.V.: 2005, The SMEI real-time data pipeline: from raw CCD frames to photometrically accurate full-sky maps. *Proc. SPIE* **5901**, 59011B. DOI.
- Hick, P.P., Buffington, A., Jackson, B.V.: 2007, A procedure for fitting point sources in SMEI white-light full-sky maps. *Proc. SPIE* **6689**, 66890C-1.
- Howard, R.A., Moses, J.D., Vourlidas, A., Newmark, J.S., Socker, D.G., Plunkett, S.P., et al.: 2008, Sun Earth Connection Coronal and Heliospheric Investigation (SECCHI). *Space Sci. Rev.* **136**, 67.
- Hunten, D.M.: 2003, Sunlit aurora and the N_2^+ ion: a personal perspective. *Planet. Space Sci.* **51**, 887.
- Jackson, B.V.: 1985, Imaging of coronal mass ejections by the Helios spacecraft. *Solar Phys.* **100**, 563.
- Jackson, B.V.: 2011, The 3D analysis of the heliosphere using interplanetary scintillation and Thomson-scattering observations. *Adv. Geosci.* **30**, 69.
- Jackson, B.V., Froehling, H.R.: 1995, Three-dimensional reconstruction of a coronal mass ejection. *Astron. Astrophys.* **299**, 885.
- Jackson, B.V., Leinert, C.: 1985, Helios images of solar mass ejections. *J. Geophys. Res.* **90**, 10759.
- Jackson, B.V., Buffington, A., Hick, P.P., Altrock, R.C., Figueroa, S., Holladay, P.E., Johnston, J.C., Kahler, S.W., Mozer, J.B., Price, S., Radick, R.R., Sagalyn, R., Sinclair, D., Simnett, G.M., Eyles, C.J., Cooke, M.P., Tappin, S.J., Kuchar, T., Mizuno, D., Webb, D.F., Anderson, P.A., Keil, S.L., Gold, R.E., Waltham, N.R.: 2004, The Solar Mass Ejection Imager (SMEI) mission. *Solar Phys.* **225**, 177.
- Jackson, B.V., Buffington, A., Hick, P.P., Wang, X., Webb, D.: 2006, Preliminary three-dimensional analysis of the heliospheric response to the 28 October 2003 CME using SMEI white-light observations. *J. Geophys. Res.* **111**(A4), A04S91.

- Jackson, B.V., Bisi, M.M., Hick, P.P., Buffington, A., Clover, J.M., Sun, W.: 2008b, Solar Mass Ejection Imager (SMEI) 3D reconstruction of the 27 – 28 May 2003 CME sequence. *J. Geophys. Res.* **113**, A00A15. DOI.
- Jackson, B.V., Hick, P.P., Bisi, M.M., Buffington, A., Clover, J.M.: 2008a, The UCSD Solar Mass Ejection Imager (SMEI) and Interplanetary Scintillation (IPS) web database, and CCMC models. In: *SHINE 08 Workshop, Zermatt, Utah, 23 – 27 June, 2008*.
- Jackson, B.V., Buffington, A., Hick, P.P., Bisi, M.M., Clover, J.M.: 2010, A heliospheric imager for deep space: lessons learned from Helios, SMEI, and STEREO. *Solar Phys.* **265**, 257. DOI.
- Jackson, B.V., Buffington, A., Cota, L., Odstrcil, D., Bisi, M.M., Fallows, R.F., Tokumaru, M.: 2020, Iterative tomography: a key to providing time-dependent 3-d reconstructions of the inner heliosphere and the unification of space weather forecasting techniques. *Front. Astron. Space Sci.* DOI.
- Jackson, B.V., Bracamontes, M.T., Buffington, A., Davies, J., Bisi, M.M., Iwai, K.: 2023, Connecting the Dots From In-Situ Spacecraft Measurements in the Global Solar Wind Filled with Mesoscale Structures. *Poster presentation at session SH23E at the AGU conference, San Francisco, California, USA, 11 – 15, December*.
- Jackson, B.V., Bracamontes, M., Pieczynski, B., Buffington, B.: 2024, Heliospheric Mesoscale 3-D Reconstructions and the UCSD Plan for the NASA Small Explorer PUNCH Analysis. *Oral presentation at the UK Space Weather and Space Environment Meeting II, Exeter, UK, 9 – 13, September*.
- Leinert, C., Richter, I., Planck, B.: 1982, Stability of the zodiacal light from minimum to maximum of the solar cycle (1974 – 1981). *Astron. Astrophys.* **110**, 111.
- Leinert, C., Link, H., Pitz, E., Salm, N., Knuppelberg, D.: 1975, Helios zodiacal light experiment. *Raumfahrtforschung* **19**, 264.
- Lummerzheim, D., Otto, A., Doe, R.A., Mizuno, D., Jackson, B.V., Webb, D.F., Collins, R.L., Light, A.S.: 2008, Observation and modeling of ion upwelling above aurora. *SA21B-1542, presented at the 2008 fall AGU, 15 – 19 December, San Francisco, California*.
- Mizuno, D.R., Buffington, A., Cooke, M.P., Eyles, C.J., Hick, P.P., Holladay, P.E., Jackson, B.V., Johnston, J.C., Kuchar, T.A., Mozer, J.B., Price, S.D., Radick, R.R., Simnett, G.M., Sinclair, D., Tappin, S.J., Webb, D.F.: 2005, Very high altitude aurora observations with the Solar Mass Ejection Imager. *J. Geophys. Res.* **110**, A07230. DOI.
- Ogilvie, K.W., Desch, M.D.: 1997, The wind spacecraft and its early scientific results. *Adv. Space Res.* **20**(445), 559.
- Richter, I., Leinert, C., Planck, B.: 1982, Search for short term variation of zodiacal light and optical detection of interplanetary plasma clouds. *Astron. Astrophys.* **110**, 115.
- Sheely, N.R. Jr., Michels, D.J., Howard, R.A., Koomen, M.J.: 1980, Initial observations with the Solwind coronagraph. *Astrophys. J.* **237**(2), L99. DOI.
- Viall, N.M., DeForest, C.E., Kepko, L.: 2021, Mesoscale structure in the solar wind. *Front. Astron. Space Sci.* **8**, 735034. DOI.

Publisher's Note Springer Nature remains neutral with regard to jurisdictional claims in published maps and institutional affiliations.

Authors and Affiliations

Bernard V. Jackson¹ · Matthew Bracamontes¹ · Andrew Buffington¹ · Stuart Volkow¹ · Stephen White² · Mario M. Bisi³ · Edward Stephan⁴ · Philippe Leblanc⁴ · Ron Quillin⁵

✉ B.V. Jackson
bvjackson@ucsd.edu

M. Bracamontes
m1bracamontes@ucsd.edu

A. Buffington
abuffington@ucsd.edu

S. Volkow
svolkow@ucsd.edu

S. White
stephen.white.24@us.af.mil

M.M. Bisi
Mario.Bisi@stfc.ac.uk

E. Stephan
ed.stephan@gmx.net

P. Leblanc
neupap@gmail.com

R. Quillin
rjquillin@gmail.com

- ¹ Department of Astronomy and Astrophysics, University of California, San Diego, La Jolla, CA 92093, USA
- ² Air Force Research Laboratory, AFRL/RVBXD, 3550 Aberdeen Ave. SE, Kirtland AFB, NM 87117, USA
- ³ RAL Space, United Kingdom Research and Innovation – Science & Technology Facilities Council - Rutherford Appleton Laboratory, RAL Space, Harwell Campus, Oxfordshire, OX11 0QX, UK
- ⁴ Stephan Design-Build, 936 Skytop Dr., Haslet, TX, 76052, USA
- ⁵ Malin Space Science Systems, 15253 Avenue of Science, San Diego, CA, USA